Universiteit
Leiden
The Netherlands

Conductance and gating effects at sputtered oxide interfaces

Yin, C.

Citation

Yin, C. (2019, July 3). *Conductance and gating effects at sputtered oxide interfaces*. *Casimir PhD Series*. Retrieved from https://hdl.handle.net/1887/74527

Version:	Not Applicable (or Unknown)
License:	Leiden University Non-exclusive license
Downloaded from:	https://hdl.handle.net/1887/74527

Note: To cite this publication please use the final published version (if applicable).

Cover Page

Universiteit Leiden

The handle http://hdl.handle.net/1887/74527 holds various files of this Leiden University dissertation.

Author: Yin, C.
Title: Conductance and gating effects at sputtered oxide interfaces
Issue Date: 2019-07-03

5

Tuning Rashba spin-orbit coupling in $LaAlO_3/SrTiO_3$ heterostructures by band filling

The electric-field tunable Rashba spin-orbit coupling at the $LaAlO_3/SrTiO_3$ interface shows potential applications in spintronic devices. However, different gate dependence of the coupling strength has been reported in experiments. On the theoretical side, it has been predicted that the largest Rashba effect appears at the crossing point of the d_{xy} and $d_{xz,yz}$ bands. In this Chapter, we study the tunability of the Rashba effect in $LaAlO_3/SrTiO_3$ by means of back-gating. The Lifshitz transition was crossed multiple times by tuning the gate voltage so that the Fermi energy is tuned to approach or depart from the band crossing. By analyzing the weak antilocalization behavior in the magnetoresistance, we find that the maximum spin-orbit coupling effect occurs when the Fermi energy is near the Lifshitz point. Moreover, we find strong evidence for a single spin winding at the Fermi surface.

An adapted version of this Chapter has been submitted for publication in a peer-reviewed journal as C. Yin, P. Seiler, L. M. K. Tang, I. Leermakers, N. Lebedev, U. Zeitler, and J. Aarts, *Tuning Rashba spin-orbit couling at $LaAlO_3/SrTiO_3$ interfaces by band filling*, arXiv preprint [149].

5.1. Introduction

Complex oxide heterostructures provide an interesting platform for novel physics since their physical properties are determined by the correlated d electrons [2]. The most famous example is the discovery of a high-mobility two-dimensional electron system (2DES) at the interface between $LaAlO_3$ and $SrTiO_3$ [9]. Intriguing properties, such as superconductivity [6], signatures of magnetism [10, 11, 15] and even their coexistence [7, 12], have been reported.

At the $LaAlO_3/SrTiO_3$ interface, the 2DES is confined in an asymmetric quantum well (QW) in $SrTiO_3$. The intrinsic structure inversion asymmetry introduces an electric field which gives rise to a Rashba spin-orbit (SO) coupling [150]. Additionally, due to the large permittivity of the $SrTiO_3$ substrate at cryogenic temperatures [123], the coupling constant can be tuned with the $SrTiO_3$ as back gate [18, 72, 74, 75]. This could give rise to applications in spintronics, such as spin field-effect transistors [151]. However, the reported results are inconsistent. Upon increasing the back-gate voltage (V_G), the SO coupling strength was found to decrease [18], increase [72, 74], or show a maximum [75]. A clear understanding of the SO coupling dependence on V_G is necessary for more advanced experiments.

For a free electron gas the Rashba spin splitting is proportional to the symmetry breaking electric field, however the Rashba effect in solids like semiconductor and oxide heterostructures has a more complicated origin [152]. Theoretical studies have shown that multiorbital effects play an essential role in the SO coupling in $LaAlO_3/SrTiO_3$ [64, 153, 154]. At the $LaAlO_3/SrTiO_3$ (001) interface, the band structure is formed by the Ti t_{2g} orbitals. At the Γ-point, the d_{xy} band lies below the $d_{xz,yz}$ bands in energy [124]. Applying V_G across the $SrTiO_3$ substrate changes the carrier density and therefore the Fermi energy (E_F). A Lifshitz transition occurs when E_F is tuned across the bottom of the $d_{xz,yz}$ bands [63]. The largest SO coupling effect was predicted at the crossing point of the d_{xy} and $d_{xz,yz}$ orbitals [64, 153, 154]. The SO coupling theory was experimentally confirmed later by angle-resolved photoemission spectroscopy (ARPES) measurements [155].

So far, few experiments actually track the evolution of SO coupling when E_F is driven to approach or depart from the Lifshitz point. In this Chapter, we study the Rashba effect in back-gated $LaAlO_3/SrTiO_3$. By carefully monitoring the sign of the magnetoresistance in high magnetic field and the linearity of the Hall resistance, V_G was tuned back and forth so that the Lifshitz transition was crossed multiple times. The SO coupling characteristic magnetic fields were extracted by fitting the weak antilocalization (WAL) behavior in the magnetoresistance (MR). We find that the maximum SO coupling effect occurs when E_F is near the Lifshitz point. We also find a single spin winding at the Fermi surface.

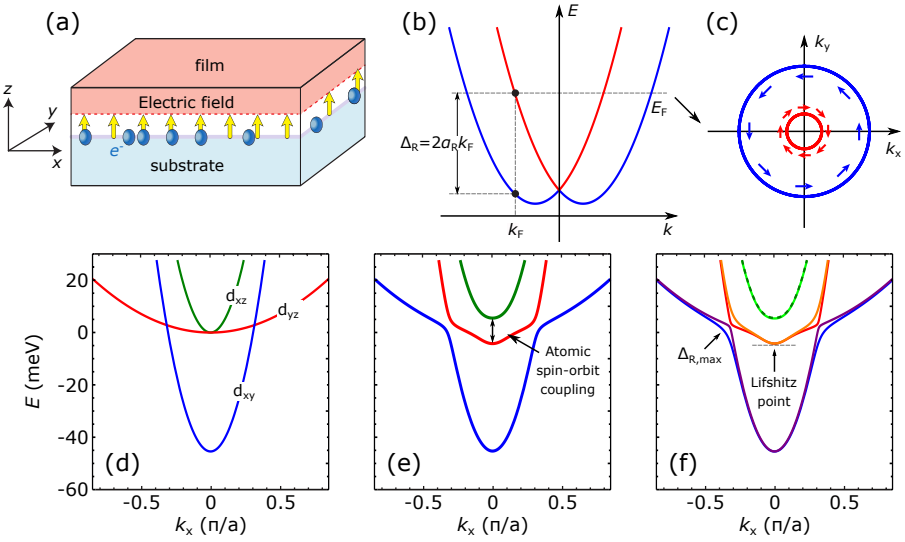

Figure 5.1: (a) Structural inversion symmetry breaking in heterostructures. The built-in electric field along the growth direction breaks the inversion symmetry, resulting in the SO coupling. (b) Band dispersion of a nearly free two-dimensional electron gas due to Rashba SO coupling. (c) The corresponding Fermi surface. The spins are locked to their momenta and counter-propagating electrons have opposite spins. Images adapted from Ref. [157]. (d)-(f) Effective three-band model at the $LaAlO_3/SrTiO_3$ interface. (d) Spin-degenerate t_{2g} bands. (e) The t_{2g} bands with atomic SO coupling included. The three bands are still double degenerate. (f) The t_{2g} bands with atomic SO coupling and inversion asymmetry included. Maximum spin splitting is at the crossing point of the d_{xy} and $d_{xz,yz}$ orbitals. The Lifshitz point is at the bottom of the $d_{xz,yz}$ bands. Images adapted from Ref. [64].

5.2. Theoretical concepts

5.2.1. Rashba spin-orbit coupling in $LaAlO_3/SrTiO_3$ heterostructures

SO coupling is most familiar in atomic physics, which describes the coupling between an electron's spin and its orbital angular momentum about the nucleus [156]. It enters into the Hamiltonian as a relativistic correction to the Schrödinger equation, giving rise to the SO term [152]

$$H_{SO} = -\frac{\hbar}{4m_e^2c^2}\vec{\sigma}\cdot\vec{p}\times\vec{\nabla}V, \tag{5.1}$$

where $\hbar$ is the Planck constant, m_e is the mass of a free electron, c is the speed of light, $\vec{\sigma} = (\sigma_x, \sigma_y, \sigma_z)$ is the vector of Pauli spin matrices, $\vec{p}$ is the kinetic momentum and V is the electric potential of the atomic core. It can be understood from Eq. (5.1) that the electric field produced by the charged nucleus gives rise to a magnetic field in the reference frame moving with an orbiting electron, resulting in a momentum-dependent effective Zeeman energy.

In condensed matter systems, electrons move in a crystal potential. SO coupling arises when there is a potential gradient on average. There are usually two types of SO couplings in condensed matter systems. The first one is the Dresselhaus SO coupling which originates from the bulk inversion asymmetry (BIA), as for instance in zinc blende structures [158]. The second one is the Rashba SO coupling which is due to the structure inversion asymmetry (SIA) in heterostructures [150]. Here we focus on the Rashba SO coupling. First, let's consider a heterostructure with a nearly free two-dimensional electron gas, as depicted in Fig. 5.1(a). The built-in electric field, $\vec{E} = E_z\vec{z}$, breaks the symmetry between the z and $-z$ direction, resulting in a Rashba SO coupling of the form [159]

$$H_R = \frac{\alpha_R}{\hbar}\vec{\sigma}\cdot\vec{p}\times\vec{z}, \tag{5.2}$$

where α_R is known as the Rashba parameter and $\vec{z}$ is the unit vector in the z direction. As shown in Fig. 5.1(b) the spin-degenerate states are split and the eigenvalues are

$$\epsilon_\pm(k) = \frac{\hbar^2k^2}{2m^*} \pm \alpha_R k, \tag{5.3}$$

where k is the wavevector and m^* is the effective mass. The spin texture at the Fermi surface is plotted in Fig. 5.1(c). The spin polarization is always perpendicular to $\vec{k}$ and counter-propagating electrons have opposite spins. The Rashba spin splitting Δ_R is given by

$$\Delta_R = 2\alpha_R k_F \tag{5.4}$$

where k_F is the Fermi wavevector. Since α_R is proportional to the interfacial electric field, it seems that Δ_R can be linearly tuned by an externally applied electric field. According to Eq. (5.4), however, a typical electric field in experiments, *e.g.* 100 V, only yields $\Delta_R \sim 10^{-8}$ meV [153], which is much smaller than the measured values at the $LaAlO_3/SrTiO_3$ interface that are of the order of meV [18, 72].

By considering the interplay between atomic SO coupling and inversion asymmetry, theoretical studies have predicted that the maximum Rashba effect is at the crossing point of the d_{xy} and $d_{xz,yz}$ orbitals [64, 153, 154], as shown in Fig. 5.1(d)-(f). In magnetotransport measurements, it is hard to estimate where the band crossing is. However, the Lifshitz point locating at the bottom of the $d_{xz,yz}$ bands is very close to the band crossing as shown in Fig. 5.1(f). Therefore, by carefully monitoring the characteristic features of the Lifshitz transition, one can nicely tune the relative position between the Fermi energy and the band crossing.

5.2.2. Weak localization and weak antilocalization effects

SO coupling can be experimentally studied from the weak antilocalization (WAL) effect in magnetotransport measurements. To understand WAL, we first introduce the weak

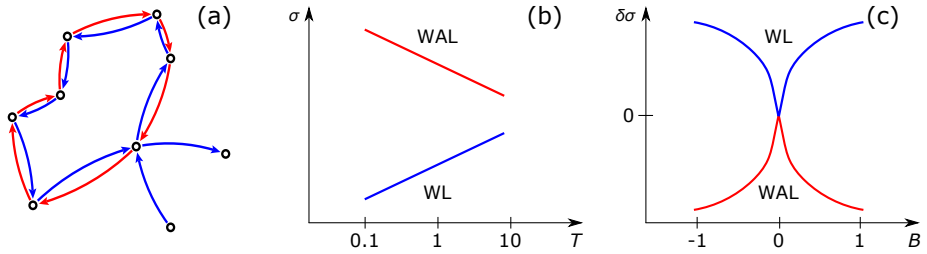

Figure 5.2: (a) Schematic of the time-reversed closed-loop trajectory pairs of electrons. The quantum interference between them becomes important when the phase coherence length is much greater than the mean free path, $l_\phi \gg l$. (b)-(c) Signatures of weak localization (WL) and weak antilocalization (WAL). (b) Temperature dependence of the conductivity σ. (c) Magnetoconductivity, $\delta\sigma = \sigma(B) - \sigma(0)$. Images adapted from Ref. [161].

localization (WL) effect. In a weakly disordered system, the electrons motion is diffusive rather than ballistic. The electronic transport is related to two characteristic lengths [160]: (i) The mean free path l, which measures the average distance that an electron travels before its momentum is changed by elastic scattering from static scattering centers. (ii) The phase coherence length l_ϕ, which measures the average distance an electron can maintain its phase coherence. l_ϕ is determined by inelastic scattering from electron-phonon and electron-electron interactions. If $l \geqslant l_\phi$, the system is in the classical diffusive regime and the conductivity is described by the Drude model. If $l \ll l_\phi$, the system is in the quantum diffusive regime since electrons maintain their phase coherence even after being scattered for many times. In this regime, the constructive quantum interference between time-reversed pairs of electrons with closed-loop trajectories, as shown in Fig. 5.2(a), will reduce the Drude conductivity. The effect of this quantum correction is called WL. In the presence of SO coupling, the electron spin is locked to its momentum. The two time-reversed paths gain an extra phase of π. The destructive quantum interfere between the two paths will then enhance the Drude conductivity. This opposite effect of WL is called WAL.

The conductivity correction from quantum interference is related to l and l_ϕ by a logarithmic function

$$\sigma^{\mathrm{qi}} \propto \pm \frac{e^2}{\pi h} \ln \frac{l_\phi}{l}, \tag{5.5}$$

where e^2/h is the conductance quantum, "$-$" corresponds to WL and "+" to WAL. In Eq. (5.5), l is determined by the elastic scattering which is temperature independent, while l_ϕ is determined by the inelastic scattering which is usually a function of temperature, and empirically, $l_\phi \propto T^{-p/2}$, where p is positive and depends on scattering mechanism and dimensionality [162]. When lowering temperature, σ^{qi} will become prominent, which gives the temperature dependence of the conductivity as shown in

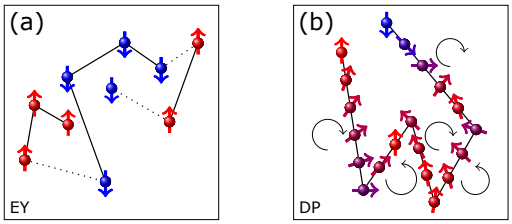

Figure 5.3: (a) Schematic of the Elliott-Yafet (EY) mechanism. Scatterings from impurities or phonons rarely flip the electron's spin. (b) Schematic of the D'yakonov-Perel' (DP) mechanism. Electron's spin continuously precesses around the internal magnetic field due to SO coupling. Arrows indicate directions of the Larmor precession. Image adapted from Ref. [170].

Fig. 5.2(b). When applying a magnetic field, the time-reversal symmetry will be broken. Since σ^{qi} is due to the quantum interference between the two time-reversed loops, it will be destroyed in a magnetic field, giving rise to the magnetoconductivity as shown in Fig. 5.2(c), which is the characteristic feature of WL and WAL.

Next, we discuss two theories for analyzing WAL, namely the HLN theory, developed by Hikami, Larkin and Nagaoka [163], and the ILP theory, developed by Iordanskii, Lyanda-Geller and Pikus [164]. The qualitative results of both theories are similar, however, the physical picture behind them are very different.

The HLN model considers the Elliott-Yafet (EY) spin relaxation mechanism [165, 166], which operates in systems with an inversion symmetry, such as silicon [167]. In the EY mechanism, the spin relaxation is due to momentum scattering from impurities or phonons. In the presence of SO coupling, the Bloch states are a mixture of spin-up and spin-down states. The degree of admixture depends on the electron's wavevector, making the electron's spin orientation dependent on its momentum. Any momentum scattering gives a probability of flipping the spin, leading to spin relaxation. The spin relaxes during the scattering as shown in Fig. 5.3(a), therefore the faster is the momentum scattering, the faster is the spin relaxation [168].

The ILP model considers the D'yakonov-Perel' (DP) spin relaxation mechanism [169], which operates in systems with a broken inversion symmetry. In the DP mechanism, SO coupling manifests itself as a momentum-dependent magnetic field. An electron moving with one velocity feels one effective magnetic field along which the electron's spin precesses. When a scattering event occurs, the electron changes it velocity and it feels a different (in both magnitude and direction) SO magnetic field. The spin performs a kind of random walk, with the spin flip occurring if the spin manages to walk as far as the opposite from its original orientation. Unlike the EY mechanism, the spin relaxes in between the scattering events as shown in Fig. 5.3(b), therefore the more scattering events there are, the less is the spin relaxation [168].

5.3. Experiments

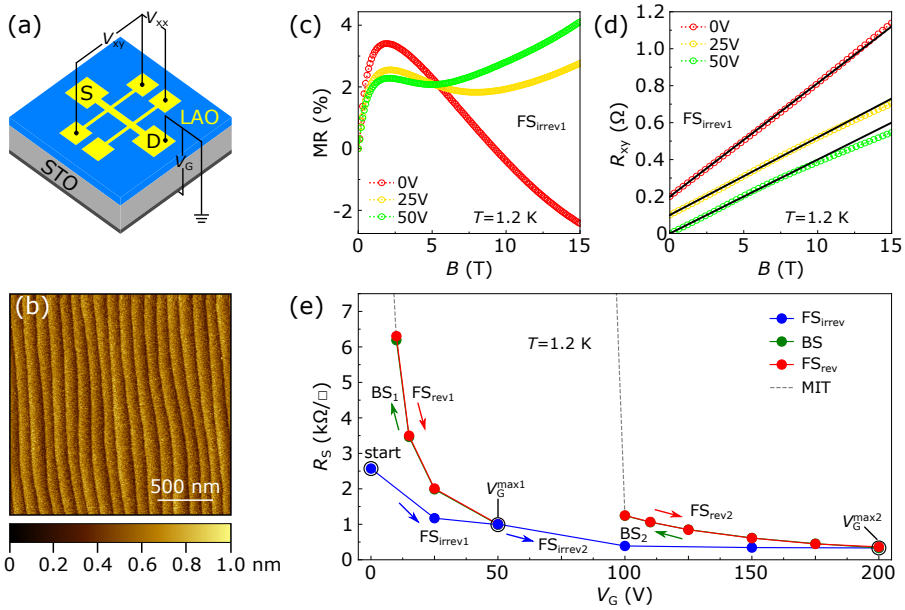

Figure 5.4: (a) Schematic of the Hall bar device. Source and drain are labeled as "S" and "D". The longitudinal voltage (V_{xx}) and transverse voltage (V_{xy}) are measured simultaneously. The gate voltage (V_G) is applied between the back of the substrate and the drain. (b) An AFM image of the $LaAlO_3$ surface taken at the Hall bar channel. (c) Magnetoresistance, MR = $[R_s(B)/R_s(0)-1]\times 100\,\%$, as a function of magnetic field, B, in the first irreversible forward sweep (FS_{irrev1}) regime at 1.2 K. (d) Hall resistance, R_{xy}, as a function of B in FS_{irrev1} at 1.2 K. Curves are separated by an offset of 100 Ω for clarity. Black lines are linear fits to $R_{xy}(B)$. (e) Sheet resistance (R_s) as a function of V_G at 1.2 K. The solid circles are $R_s(B=0)$. The blue, green and red arrows indicate the irreversible forward sweep (FS_{irrev}), backward sweep (BS), and reversible forward sweep (FS_{rev}), respectively. Two BSs were performed at 50 V (V_G^{max1}) and 200 V (V_G^{max2}). The gray dashed line indicates the metal-insulator transition (MIT).

The back-gating experiments were performed on a Hall bar device as depicted in Fig. 5.4(a). The Hall bar pattern was fabricated by photolithography as discussed in Chapter 2. The length between two voltage probes is 1000 µm, and the Hall bar width is 150 µm. 15 unit cells of $LaAlO_3$ film were deposited at 800 °C and an Ar pressure of 0.04 mbar by 90° off-axis sputtering. Fig. 5.4 (b) shows an AFM image of the $LaAlO_3$ surface. The back-gate electrode was formed by uniformly applying a thin layer of silver paint (Ted Pella, Inc.) on the back of the substrate. Magnetotransport measurements were performed under different V_G at 1.2 K in the Nijmegen cryostat. The longitudinal voltage (V_{xx}) and transverse voltage (V_{xy}) were measured simultaneously by standard lock-in technique (f = 13.53 Hz and i_{RMS} = 1.0 µA). The maximum applied V_G was +200 V and the leakage

current was less than 1 nA during the measurement.

The device was first cooled down to 1.2 K with V_G grounded. In the original state (V_G = 0 V), the observed maximum in MR (Fig 5.4(c)) in low magnetic fields shows the signature of WAL [72]. The negative MR in high magnetic fields as well as the approximately linear Hall resistance (R_{xy}) (Fig 5.4(d)) indicate that the presence of only one type of carriers. Next, V_G was increased to add electrons to the QW and two characteristic Lifshitz transition features appeared at 25 V. They are the emergence of positive MR in high magnetic field and the change of linearity of $R_{xy}(B)$ [63, 89]. V_G was further increased to 50 V (V_G^{max1}) to drive E_F slightly above the Lifshitz point, resulting in larger positive MR and more downward bending of R_{xy} in high magnetic fields.

Then V_G was decreased to remove electrons from the QW in order to go back through the Lifshitz transition from the high-density direction. In Chapter 4, we have shown that due to the effect of electron trapping in $SrTiO_3$, the sheet resistance (R_s) always follows an irreversible route when V_G is first swept forward and then backward. Fig. 5.4(e) shows R_s as a function of V_G. It can be seen that R_s increases above the virgin curve when V_G is swept backward. The backward sweep finally leads to a metal-insulator transition (MIT), whose onset is defined from the phase shift of the lock-in amplifier increasing above 15°. Sweeping V_G forward again results in a reversible decrease of R_s which overlaps with the previous backward sweep and the system is fully recovered when V_G is reapplied to 50 V. We therefore classify V_G sweeps into three regimes, namely irreversible forward sweep (FS_{irrev}), backward sweep (BS) and reversible forward sweep (FS_{rev}). V_G was then increased to 200 V (V_G^{max2}) to drive E_F well above the Lifshitz point. Similar reversible behavior is observed in BS_2 and FS_{rev2}.

5.4. Back-gate tuning of magnetotransport properties

Fig. 5.5(a)-(h) demonstrate the back-gate tuning of magnetotransport properties in various regimes. Besides the signature of WAL and characteristic features of the Lifshitz transition, we also observed small upturns in R_{xy} in intermediate magnetic fields. The Hall coefficient, $R_H = R_{xy}/B$ in various regimes is plotted in Fig. 5.5(i)-(l). A similar feature has also been reported by other groups [63, 171], but its origin is still under debate. There are attempts to relate it to an unconventional anomalous Hall effect (AHE) [172] or hole transport [171], however we cannot get convincing fits using these models. To extract the carrier density and mobility as a function of V_G, we fitted the magnetotransport data with a two-band model [128]

$$R_s = \frac{1}{e} \cdot \frac{\frac{n_1\mu_1}{1+(\mu_1 B)^2} + \frac{n_2\mu_2}{1+(\mu_2 B)^2}}{\left(\frac{n_1\mu_1}{1+(\mu_1 B)^2} + \frac{n_2\mu_2}{1+(\mu_2 B)^2}\right)^2 + \left(\frac{n_1\mu_1^2 B}{1+(\mu_1 B)^2} + \frac{n_2\mu_2^2 B}{1+(\mu_2 B)^2}\right)^2}, \tag{5.6}$$

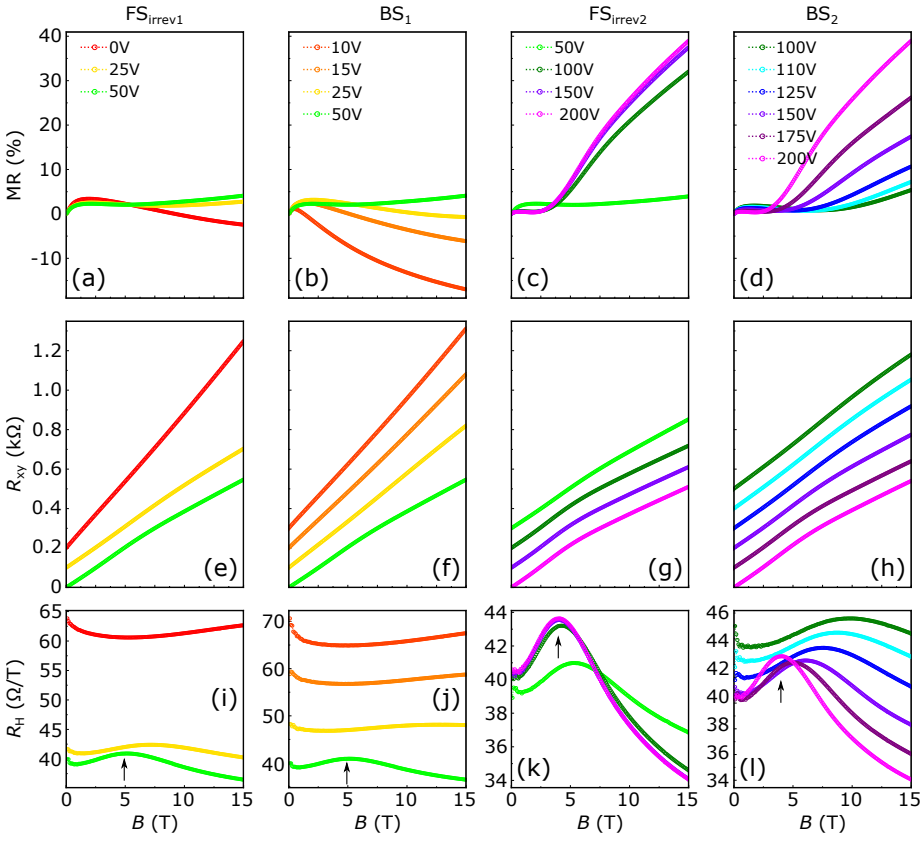

Figure 5.5: (a)-(d) Magnetoresistance, MR, as a function of magnetic field, B, in various regimes: (a) FS$_{irrev1}$, (b) BS$_1$, (c) FS$_{irrev2}$ and (d) BS$_2$. (e)-(h) Hall resistance, R_{xy}, as a function of B in various regimes: (e) FS$_{irrev1}$, (f) BS$_1$, (g) FS$_{irrev2}$ and (h) BS$_2$. Curves are separated by an offset of 100 Ω for clarity. (i)-(l) Hall coefficient, $R_H = R_{xy}/B$, as a function of B in various regimes: (i) FS$_{irrev1}$, (j) BS$_1$, (k) FS$_{irrev2}$ and (l) BS$_2$. Black arrows indicate the small upturns in R_{xy}. The results of FS$_{rev}$ regimes are similar to that of BS regimes, which are therefore omitted.

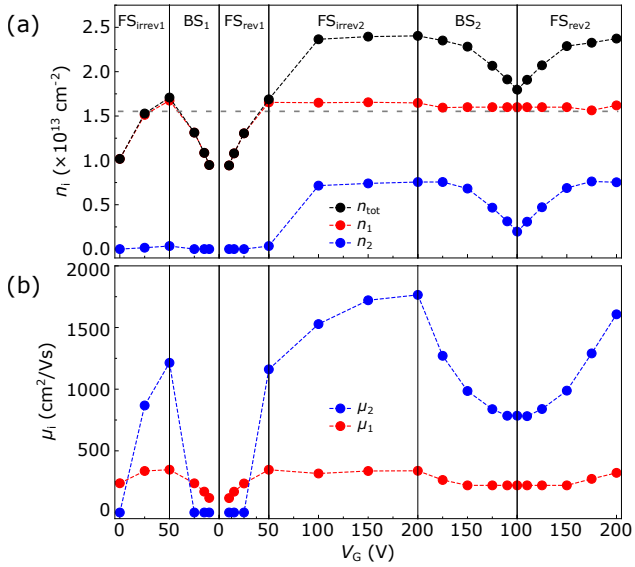

Figure 5.6: (a) V_G dependence of carrier densities. n_1 and n_2 stand for that of the low mobility carriers (LMC) and high mobility carriers (HMC), respectively. The total carrier density (n_{tot}) is the sum of n_1 and n_2. The gray dash line represent the critical carrier density ($n_L = 1.51 \times 10^{13}$ cm^{-2}) for Lifshitz transition. (b) V_G dependence of mobilities, that of the LMC and HMC are labeled as μ_1 and μ_2, respectively.

$$R_{xy} = \frac{B}{e} \frac{\frac{n_1\mu_1^2}{1+\mu_1^2B^2} + \frac{n_2\mu_2^2}{1+\mu_2^2B^2}}{(\frac{n_1\mu_1}{1+\mu_1^2B^2} + \frac{n_2\mu_2}{1+\mu_2^2B^2})^2 + (\frac{n_1\mu_1^2B}{1+\mu_1^2B^2} + \frac{n_2\mu_2^2B}{1+\mu_2^2B^2})^2}, \tag{5.7}$$

where n_1 and n_2 are the carrier densities of the first and second conduction bands, respectively, and μ_1 and μ_2 are the corresponding mobilities. For a reliable convergence n_2 and μ_2 are set to 0 in the one-band transport regime. We note that n_1 has the d_{xy} character and n_2 has the $d_{xz,yz}$ character. The total carrier density, n_{tot}, is the sum of n_1 and n_2. The small upturns in R_{xy} cannot be captured by the two-band model, however, we emphasize that the extraction of the transport parameters is not affected strongly by this feature.

As shown in Fig. 5.6(a), the critical carrier density (n_L) corresponding to the Lifshitz transition is 1.51×10^{13} cm^{-2}, which is close to earlier reported results [63]. The evolution of the carrier densities indicates that E_F approaches the Lifshitz point in regimes FS$_{irrev1}$, FS$_{rev1}$ and BS$_2$ and departs from the Lifshitz point in regimes BS$_1$, FS$_{irrev2}$ and FS$_{rev2}$. In Fig. 5.6(b), it can be seen that μ_1 almost stays unaffected above the Lifshitz transition whereas μ_2 can be considerably changed tuned by V_G, reaching ~1800 cm^2/Vs at 200 V.

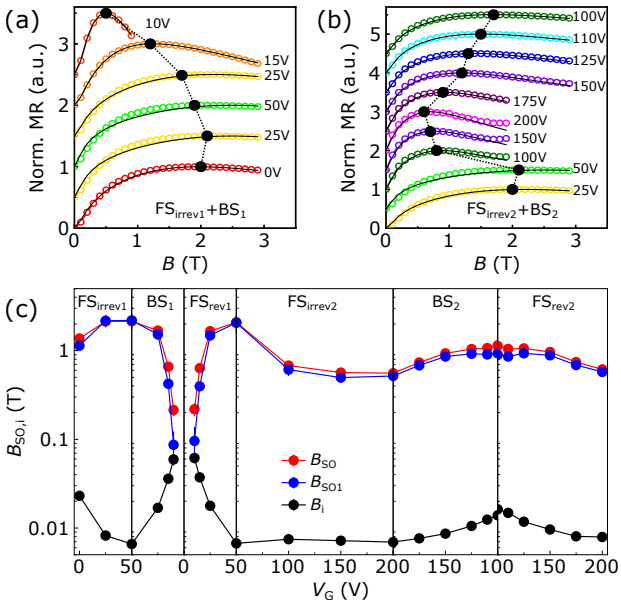

Figure 5.7: (a)-(b) Weak antilocalization (WAL) analysis of the magnetoresistance (MR) in regimes (a) FS$_{irrev1}$ and BS$_1$ and (b) FS$_{irrev2}$ and BS$_2$. The solid circles correspond to experimental data and black lines to fits using the ILP model. The local maximum of each MR curve is plotted black. The MR curves are normalized to the local maxima and separated by an offset of 0.5. The black dashed line is a guide to the eye for the evolution of the local maxima. (c) Fitted characteristic magnetic fields as a function of V_G. SO field B_{SO} is the sum of B_{SO1} (single spin winding) and B_{SO3} (triple spin winding). B_i is the inelastic scattering field. WAL analyses were performed by P. Seiler.

5.5. Weak antilocalization analysis

In low-dimensional systems, the conductivity shows signatures of quantum interference between time-reversed closed-loop electron trajectory pairs. In the presence of SO coupling the pairs interfere destructively, leading to a positive MR in low magnetic field which is known as the WAL [173]. For a system with Rashba-type of SO coupling, the spin relaxation is described by the DP mechanism [169]. The model for analyzing the WAL was established by Iordanskii, Lyanda-Geller and Pikus (ILP) [164]. In this model, both the single and triple spin winding contributions at the Fermi surface have been taken into account. It should be noted that the ILP model is an effective single-band model, which means that above the Lifshitz point the fitted characteristic magnetic field for SO coupling is an effective field for both the d_{xy} and $d_{xz,yz}$ bands. A model that considers multi-band effects is not available yet. The WAL correction to the magnetoconductivity

is given by [164, 171, 174, 175]:

$$\Delta\sigma(B) = -\frac{e^2}{2\pi h}[\mathscr{L}(B) - \mathscr{L}(0) + \psi(\frac{1}{2} + \frac{B_\mathrm{i}}{B}) - \ln(\frac{B_\mathrm{i}}{B})], \tag{5.8}$$

where ψ is the digamma function, and

$$\mathscr{L}(B) = \frac{1}{a_0} + \frac{2a_0 + 1 + \frac{B_{\mathrm{SO1}}+B_{\mathrm{SO3}}}{B}}{a_1(a_0 + \frac{B_{\mathrm{SO1}}+B_{\mathrm{SO3}}}{B}) - 2\frac{B_{\mathrm{SO1}}}{B}} + \sum_{n=1}^{\infty} \frac{3a_n^2 + 2a_n\frac{B_{\mathrm{SO1}}+B_{\mathrm{SO3}}}{B} - 1 - 2(2n+1)\frac{B_{\mathrm{SO1}}}{B}}{(a_n + \frac{B_{\mathrm{SO1}}+B_{\mathrm{SO3}}}{B})a_{n-1}a_{n+1} - 2\frac{B_{\mathrm{SO1}}}{B}[(2n+1)a_n - 1]}, \tag{5.9}$$

where

$$a_n = n + \frac{1}{2} + \frac{B_\mathrm{i} + B_{\mathrm{SO1}} + B_{\mathrm{SO3}}}{B}. \tag{5.10}$$

The fitting parameters are the characteristic magnetic fields for the inelastic scattering $B_\mathrm{i} = \hbar/4eD\tau_\mathrm{i}$, and for the spin-orbit coupling $B_{\mathrm{SO}\,n} = (\hbar/4eD)2\Omega_n^2\tau_n$ ($n = 1$ or 3 for single or triple spin winding), where D is the diffusion constant, τ_i and τ_n are relaxation times, and Ω_n is spin splitting coefficient.

Fig. 5.7(a) and 5.7(b) depict WAL fits of the MR in the two $\mathrm{FS_{irrev}}$ and BS regimes. The solid black circles represent the local maxima of the MR curves. In principle, the SO coupling strength can be roughly estimated by the magnetic field ($B_{\max}$) where the local maximum appears [75]. It can be clearly seen that $B_{\max}$ increases as E_F approaches the Lifshitz point (regimes $\mathrm{FS_{irrev1}}$ and $\mathrm{BS_2}$), while $B_{\max}$ decreases as E_F departs from the Lifshitz point (regimes $\mathrm{BS_1}$ and $\mathrm{FS_{irrev2}}$). The fitted values for the characteristic magnetic fields are plotted in Fig. 5.7(c), where B_SO is the sum of B_{SO1} and B_{SO3}. In most cases B_{SO3} is much smaller than B_{SO1}, indicating a single spin winding at the Fermi surface. It can be seen that B_{SO1} rises almost an order of magnitude in $\mathrm{FS_{rev1}}$, and then goes down by a factor of 2 in $\mathrm{FS_{irrev2}}$. The maximum SO coupling strength occurs near the Lifshitz point, agreeing with the evolution of $B_{\max}$. Driving E_F either above or below the Lifshitz point would lead to a decrease of the SO coupling strength. B_i increases when the carrier density is lowered, which is due to more accessible phonons contributing to the scattering process, and vice versa.

If B_{SO1} is 0 and only B_{SO3} is present, the ILP formula could be reduced to the simpler model developed by Hikami, Larkin and Nagaoka (HLN) [163], in which the spin relaxation is described by the EY mechanism [165, 166]. However, the HLN model yields inaccurate fits to our data, which is different from earlier reported results [75, 176], where a triple spin winding has been found. We also tried the model suggested by Maekawa and Fukuyama (MF) [177], which takes the Zeeman splitting into account. However, the MF model also gives inaccurate fits. Fig. 5.8(a)-(c) show the comparison between the fitting

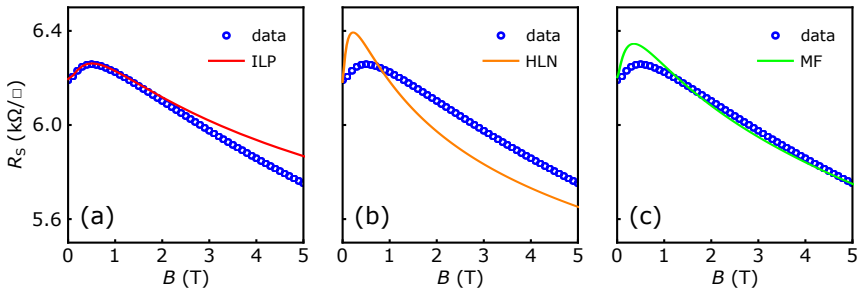

Figure 5.8: WAL analysis to the MR curve measured at 10 V in BS_1 from different models. (a) ILP model. (b) HLN model. (c) MF model. WAL analyses were performed by P. Seiler.

results from the three models. The WAL feature in low magnetic fields is nicely caught by the ILP model.

5

5.6. Conclusion

In summary, we have performed magnetotransport measurements to study the Rashba spin-orbit couping effect in back-gated $LaAlO_3/SrTiO_3$. By tuning the gate voltage, the Fermi energy has been driven to approach or depart from the Lifshitz point multiple times. We have done weak antilocalization analysis of the magnetoresistance using the ILP model, which reveals a single spin winding at the Fermi surface. We have found that the maximum Rashba effect occurs when the Fermi energy is near the Lifshitz point, and that the change of the characteristic field on the low carrier density side is larger than the high carrier density side. Our experiments have manifested the nontrivial Rashba effect predicted by theoretical works. Applying an external electric field can tune the coupling strength, but its direct contribution is rather small. Instead the gating effect is indirect. It is the tuning of carrier densities and therefore band filling that significantly influence the Rashba effect. Driving the Fermi energy above or below the Lifshitz point would result in a decrease of the coupling strength. Our findings provide valuable insights to the investigation and design of oxide-based spintronic devices.